ACS APPLIED MATERIALS & INTERFACES

Research Article

www.acsami.org

Facile One-Pot Synthesis of Fe_3O_4@Au Composite Nanoparticles for Dual-Mode MR/CT Imaging Applications

Jingchao Li,[†,⊥] Linfeng Zheng,[‡,⊥] Hongdong Cai,[§] Wenjie Sun,[†] Mingwu Shen,*[,†] Guixiang Zhang,*[,‡] and Xiangyang Shi*[,†,§,∥]

[†]College of Chemistry, Chemical Engineering and Biotechnology, Donghua University, Shanghai 201620, P. R. China

[‡]Department of Radiology, Shanghai First People's Hospital, School of Medicine, Shanghai Jiaotong University, Shanghai 200080, P. R. China

[§]State Key Laboratory for Modification of Chemical Fibers and Polymer Materials, College of Materials Science and Engineering, Donghua University, Shanghai 201620, P. R. China

[∥]CQM-Centro de Química da Madeira, Universidade da Madeira−Campus da Penteada, Funchal 9000-390, Portugal

Supporting Information

ABSTRACT: A facile one-pot hydrothermal approach to synthesizing Fe_3O_4@Au composite nanoparticles (CNPs) for dual-mode magnetic resonance (MR) and computed tomography (CT) imaging applications is reported. In this work, polyethyleneimine (PEI) partially modified with poly(ethylene glycol) monomethyl ether (*m*PEG) was used as a stabilizer to form gold NPs (*m*PEG-PEI.NH_2-Au NPs) with the assistance of sodium borohydride reduction. The *m*PEG-PEI.NH_2-Au NPs were then mixed with iron(II) salt in a basic aqueous solution followed by treatment under an elevated temperature and pressure. This hydrothermal process led to the formation of Fe_3O_4@Au-*m*PEG-PEI.NH_2 CNPs. The remaining PEI amine groups were finally acetylated to reduce the surface positive charge of the CNPs. The formed Fe_3O_4@Au-*m*PEG-PEI.NHAc (Fe_3O_4@Au) CNPs were characterized via different techniques. The combined in vitro cell viability assay, cell morphology observation, flow cytometry, and hemolysis assay data show that the formed Fe_3O_4@Au CNPs are noncytotoxic and hemocompatible in the given concentration range. MR and CT imaging data reveal that the formed Fe_3O_4@Au CNPs have a relatively high r_2 relaxivity (146.07 mM^{-1} s^{-1}) and good X-ray attenuation property, which enables their uses as contrast agents for MR imaging of mouse liver and CT imaging of rat liver and aorta. The Fe_3O_4@Au CNPs developed via the facile one-pot approach may have promising potential for the dual-mode MR/CT imaging of different biological systems.

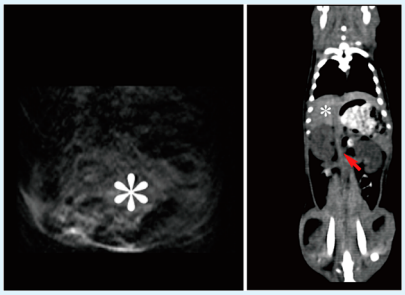

KEYWORDS: *iron oxide nanoparticles, gold nanoparticles, magnetic resonance imaging, computed tomography imaging, hydrothermal synthesis*

INTRODUCTION

Molecular imaging techniques including magnetic resonance (MR) imaging,[1−4] position emission tomography (PET) imaging,[5,6] computed tomography (CT) imaging,[7−10] optical imaging,[11,12] and single photon emission computed tomography imaging[13−15] have been demonstrated to have promising potential in disease diagnosis by visualizing cellular function and the followup of molecular processes in living organisms. However, each of the imaging modalities possesses its intrinsic limitations and weaknesses, and none of them is able to provide complete structural and functional information independently.[16] Therefore, it is highly desirable to develop dual-mode molecular imaging techniques, such as MR/fluorescence,[17,18] MR/PET,[19,20] CT/PET,[21,22] MR/CT,[23−25] CT/NIR fluorescence,[26] or MR/optical imaging,[27−29] for more accurate diagnosis of disease. Among different molecular imaging techniques, MR imaging is a powerful noninvasive imaging technique because of its good temporal and spatial resolution, nonionizing radiation source, and long effective imaging windows,[2,30,31] whereas CT imaging is another reliable molecular imaging mode that has been widely used in clinical disease diagnosis for more than half of a century because of its greater spatial and density resolution than other imaging modalities. It is reasonable to combine both the MR and CT imaging modalities together for accurate disease diagnosis.

Recent advances in nanotechnology show that various nanoparticles (NPs) can be used as contrast agents for molecular imaging applications.[1−15,32] Among the developed NP systems, superparamagnetic iron oxide (Fe_3O_4) NPs have been extensively explored as a negative contrast agent for T_2-weighted MR imaging applications.[2,33−36] On the other hand, gold (Au) NPs have been widely used for different biomedical applications,[9,37−39] especially as a kind of novel contrast agent for CT imaging because of their good biocompatibility and high

Received: August 17, 2013
Accepted: September 24, 2013
Published: September 24, 2013

Scheme 1. Schematic Illustration of the Hydrothermal Synthesis of Fe_3O_4@Au CNPs

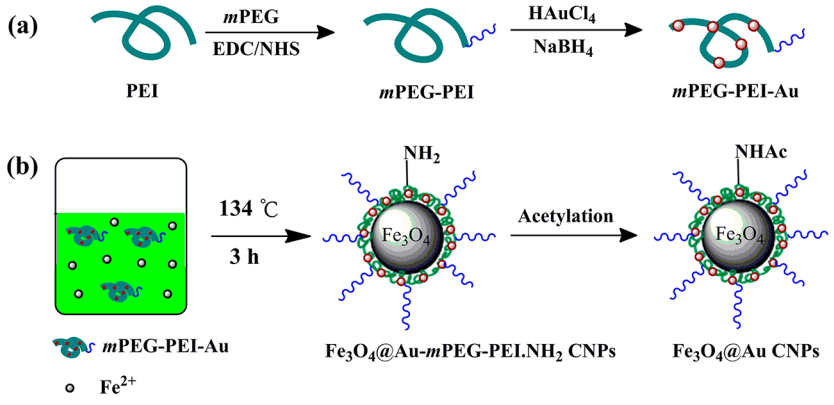

X-ray attenuation coefficient.[10,23,25,40−43] With the emergence of advanced synthetic nanotechnology, various composite nanoparticles (CNPs) consisting of both Fe_3O_4 and Au components have been synthesized. For instance, Xu et al.[44] reported the synthesis of Fe_3O_4@Au dumbbell NPs by decomposing iron pentacarbonyl on the surfaces of Au NPs in the presence of oleic acid and oleylamine followed by subsequent functionalization via a surfactant exchange process. Zhang et al.[45] prepared Fe_3O_4/polypyrrole (PPy)/Au core/shell/shell NPs by coating PPy onto preformed Fe_3O_4 NPs through the chemical oxidative polymerization of pyrrole and subsequent assembly of plentiful Au NPs on the surface of Fe_3O_4/PPy. Maleki et al.[46] adopted a water-in-oil nanoemulsion process to prepare monodisperse Fe_3O_4 NPs, and then fabricated Fe_3O_4@Au CNPs by conformal coating of the Fe_3O_4 NPs with a thin shell of Au NPs through chemical reduction of attached $HAuCl_4$ on the surface of the synthesized Fe_3O_4 NPs. The formed Fe_3O_4@Au CNPs have good colloidal stability. However, most of the formed Fe_3O_4@Au CNPs have not been used for dual-mode MR/CT imaging applications.[24]

In our previous work, we have shown that Fe_3O_4@Au CNPs synthesized via a dendrimer-mediated layer-by-layer (LbL) self-assembly process possess both excellent r_2 relaxivity of Fe_3O_4 NPs and high X-ray attenuation intensity of Au NPs.[47] The coexistence of Fe_3O_4 NPs and Au NPs within one CNP system enables dual-mode MR/CT imaging applications. However, the synthesis of the CNP system involves multiple assembly steps and requires preformed Fe_3O_4 NPs and dendrimer-entrapped Au NPs. The development of an Fe_3O_4@Au particulate system with good water dispersibility and colloidal stability via a simple route is still in high demand.

Recently, we have shown that a unique one-pot hydrothermal approach can be used to synthesize Fe_3O_4 NPs,[48] 3-aminopropyltrimethoxysilane (APTS)-coated Fe_3O_4 (Fe_3O_4@APTS) NPs,[36] and polyethyleneimine (PEI)-coated Fe_3O_4 (Fe_3O_4-PEI) NPs[33] with good water dispersibility and colloidal stability. Furthermore, the formed Fe_3O_4@APTS or Fe_3O_4-PEI NPs can be further modified to have different surface functionalities for biomedical applications.[33,35,36] In another work, we have shown that PEI can be used as an efficient stabilizer to synthesize Au NPs.[49,50] These prior successes lead us to hypothesize that it is possible to fabricate Fe_3O_4@Au CNPs via a facile one-pot hydrothermal route.

In this present study, a facile one-pot hydrothermal approach was developed to synthesize Fe_3O_4@Au CNPs for dual-mode MR/CT imaging applications (Scheme 1). In this work, PEI was first partially modified with poly(ethylene glycol) monomethyl ether (*m*PEG) to obtain the *m*PEG-PEI.NH_2 conjugate, which was subsequently used as a stabilizer to synthesize Au NPs (*m*PEG-PEI.NH_2-Au NPs) via the sodium borohydride ($NaBH_4$) reduction of $HAuCl_4$ in aqueous solution at room temperature. The formed *m*PEG-PEI.NH_2-Au NPs were then mixed with Fe(II) salt in a basic aqueous solution and autoclaved under an elevated temperature and pressure. This hydrothermal synthesis led to the formation of Fe_3O_4@Au-*m*PEG-PEI.NH_2 CNPs with abundant PEI surface amines. Finally, the remaining PEI surface amines were acetylated to reduce the surface positive charge of the CNPs. The as-synthesized Fe_3O_4@Au-*m*PEG-PEI.NHAc (Fe_3O_4@Au) CNPs were characterized via different techniques. The T_2 relaxometry and X-ray absorption coefficient of the CNPs were measured to evaluate their MR and CT imaging potential. A cell viability assay, flow cytometry, cell morphology observation, and hemolytic assay were adopted to assess the cytotoxicity and hemocompatibility of the CNPs. Finally, MR imaging of mouse liver and CT imaging of rat liver and aorta were performed to verify their dual-mode MR/CT imaging capability by intravenous injection of the Fe_3O_4@Au CNPs. To our knowledge, this is the first report related to the fabrication of Fe_3O_4@Au CNPs by a facile one-pot hydrothermal route for dual-mode MR/CT imaging applications.

EXPERIMENTAL SECTION

Materials. Ammonia (25−28% NH_3 solution in water), ferrous chloride tetrahydrate ($FeCl_2{\cdot}4H_2O$ > 99%), PEI (M_w = 25 000), and $NaBH_4$ were from Aldrich (St. Louis, MO). *m*PEG with a carboxyl end group was purchased from Shanghai Yanyi Biotechnology Corporation (Shanghai, China). 1-Ethyl-3-[3-dimethylaminopropyl] carbodiimide hydrochloride (EDC), *N*-hydroxysuccinimide (NHS), and fluorescein diacetate (FDA) were supplied by J&K Chemical Ltd (Shanghai, China). KB cells (a human epithelial carcinoma cell line) were acquired from the Institute of Biochemistry and Cell Biology, the Chinese Academy of Sciences (Shanghai, China). RPMI 1640 medium, penicillin, streptomycin, and fetal bovine serum (FBS) were purchased from Hangzhou Jinuo Biomedical Technology (Hangzhou, China). 3-(4,5-Dimethylthiazol-2-yl)-2,5-diphenyltetrazolium bromide (MTT) was purchased from Shanghai Sangon Biological Engineering Technology & Services Co., Ltd (China). $HAuCl_4{\cdot}4H_2O$, acetic anhydride, triethylamine, and all other chemicals and solvents were from Sinopharm Chemical Reagent Co., Ltd (Shanghai, China). All chemicals were used as received without further purification. The water used in all experiments was purified via a Milli-Q Plus 185 water purification system (Millipore, Bedford, MA) to have a resistivity higher than 18.2 MΩ cm. Regenerated cellulose dialysis membranes (MWCO = 14 000) were provided by Fisher.

Partial Surface Modification of PEI with *m*PEG. For the surface modification of PEI with *m*PEG, the carboxyl group of *m*PEG was first activated according to our previous work.[25] Briefly, *m*PEG (60 mg) dissolved in water (5.0 mL) with 15 molar equiv of PEI was reacted with a mixture of EDC (19.17 mg) and NHS (11.51 mg) in 2.0 mL of water solution under vigorous magnetic stirring for 3 h. The activated *m*PEG was then added dropwise into an aqueous solution of PEI (50 mg, 10 mL) under vigorous magnetic stirring, and the reaction was continued for 3 days at room temperature. Finally, the reaction mixture was dialyzed against water (nine times, 2 L) for 3 days through a membrane with MWCO of 14 000 to obtain the purified *m*PEG-PEI.NH_2 conjugate.

Synthesis of *m*PEG-PEI.NH_2-Au NPs. The synthesized *m*PEG-PEI.NH_2 conjugate was used as a stabilizer to synthesize Au NPs according to the protocol reported in our previous work, with the PEI/gold salt molar ratio of 1:200.[51] Briefly, an $HAuCl_4$ aqueous solution (30 mg/mL, 5.4 mL) was added into the water solution of *m*PEG-PEI.NH_2 (containing 50 mg of PEI) under vigorous magnetic stirring. After 30 min, an ice-cold $NaBH_4$ solution (45.4 mg, 0.9 mL in water/ethanol, v/v 2:1) was added into the $HAuCl_4$/*m*PEG-PEI.NH_2 mixture solution under vigorous stirring. The reaction mixture turned deep red within a few seconds after the addition of the $NaBH_4$ solution. The stirring process was continued for 2 h to complete the reaction. The reaction mixture was then dialyzed against water (nine times, 2 L) for 3 days through a membrane with MWCO of 14 000 to remove the excess reactants and byproducts. The obtained *m*PEG-PEI.NH_2-Au NPs were redispersed in water and stored at 4 °C for further use.

Synthesis of Fe_3O_4@Au-*m*PEG-PEI.NH_2 CNPs. The Fe_3O_4@Au-*m*PEG-PEI.NH_2 CNPs were synthesized using a facile one-pot approach following protocols reported in the literature with a slight modification.[33] In brief, $FeCl_2{\cdot}4H_2O$ (125 mg) was dissolved in water (2.0 mL). Ammonium hydroxide (0.625 mL) was added to the above solution under vigorous stirring, and the suspension was continuously stirred in air for about 10 min to allow the iron(II) to be oxidized. When the solution turned dark, the reaction mixture was transferred to a 50 mL Teflon-sealed stainless steel autoclave (KH-50 autoclave, Shanghai Yuying Instrument Co., Ltd., Shanghai). The suspension of *m*PEG-PEI.NH_2-Au NPs (containing 50 mg PEI) was then added into the autoclave. After thorough stirring, the reaction mixture was autoclaved at 134 °C and 2 bar. After 3 h, the mixture was set aside and cooled to room temperature. The precipitate was then collected by settlement with an external magnet and purified 5 times with water to remove the existing excess reactants and byproducts. Finally, the obtained Fe_3O_4@Au-*m*PEG-PEI.NH_2 CNPs were redispersed in water (10 mL).

Acetylation of Fe_3O_4@Au-*m*PEG-PEI.NH_2 CNPs. The positively charged PEI amine groups on the surface of the Fe_3O_4@Au-*m*PEG-PEI.NH_2 CNPs were then neutralized by an acetylation reaction according to a method reported in our previous work.[42,52] In brief, triethylamine (12 μL) was added to an aqueous solution of Fe_3O_4@Au-*m*PEG-PEI.NH_2 CNPs (5 mL, containing approximately 25 mg of PEI), and the solution was mixed well for 30 min. Acetic anhydride (7 μL) dispersed in 2 mL of methanol was then added dropwise into the Fe_3O_4@Au-*m*PEG-PEI.NH_2 CNPs/triethylamine mixture solution under vigorous magnetic stirring, and the reaction was continued for 24 h at room temperature. Afterward, five cycles of centrifugation/washing/redispersion were performed to remove the excess reactants and byproducts. The final Fe_3O_4@Au-*m*PEG-PEI.NHAc (Fe_3O_4@Au) CNPs were then obtained and dispersed in 5 mL of water before use.

Characterization Techniques. A Bruker AV400 nuclear magnetic resonance spectrometer was used to acquire ^1H NMR spectra. D_2O was used as a solvent to dissolve the samples before the experiments. A Lambda 25 UV−vis spectrophotometer (PerkinElmer, Boston, MA) was used to collect the UV−vis spectra. The samples were dispersed in water before measurements. X-ray diffraction (XRD) was used to characterize the crystalline structure of the Fe_3O_4@Au CNPs in a 2θ range of 20−90°. Step scans were performed using a D/max 2550 PC X-ray diffractometer (Japan, Rigaku Cop.) with Cu Kα radiation (λ = 0.154056 nm) at 40 kV and 200 mA. Thermogravimetric analysis (TGA) was used to characterize the composition of the Fe_3O_4@Au CNPs using a TG 209 F1 (Netzsch Instruments Co., Ltd., Germany) thermogravimetric analyzer. Samples were heated from 25 to 700 °C at a heating rate of 20 °C/min under a nitrogen atmosphere. A Malvern Zetasizer Nano ZS model ZEN3600 (Worcestershire, U.K.) equipped with a standard 633 nm laser was used to measure the zeta potential and hydrodynamic size of the formed Fe_3O_4@Au-*m*PEG-PEI.NH_2 CNPs and Fe_3O_4@Au CNPs. Furthermore, the Fe_3O_4@Au CNPs were dispersed in water, PBS, and RPMI 1640 medium containing FBS for a period of time up to 1 month to check the colloidal stability of the particles. The size and morphology of the formed Fe_3O_4@Au CNPs were characterized by TEM imaging (JEOL 2010F analytical electron microscope) at an operating voltage of 200 kV. TEM samples were prepared by placing 1 drop of the diluted particle suspension (5 μL) onto a carbon-coated copper grid, and the particle suspension was air-dried before measurements.

To determine the Fe and Au composition in the Fe_3O_4@Au CNPs, a Leeman Prodigy inductively coupled plasma−atomic emission spectroscopy (ICP−AES) system (Hudson, NH) was used. The CNP suspension was treated with aqua regia (250 μL) and diluted before analysis. The T_2 relaxometry of the Fe_3O_4@Au CNPs was performed using an NMI20-Analyst NMR analyzing and imaging system (Shanghai Niumag Corporation, China). The samples were diluted with water in 2 mL eppendorf tubes to have different Fe concentrations (0.005−0.16 mM) before the measurements were taken. A CPMG sequence was used to measure the T_2 relaxation times. Ten echoes in total were used with the following parameters: magnet field = 0.55 T, point resolution = 156 mm ×156 mm, section thickness = 0.6 mm, TR = 6000 ms, TE = 100 ms, and excitation number = 1. The T_2 relaxivity was calculated by a linear fit of the inverse T_2 ($1/T_2$) relaxation time as a function of the Fe concentration. A GE LightSpeed VCT imaging system (GE Medical Systems) was used for the CT scanning of the samples with 100 kV, 80 mA, and a slice thickness of 0.625 mm. The samples dispersed in water with different Au concentrations (0.01−0.06 M) were put into 2 mL eppendorf tubes and placed in a self-designed scanning holder. Evaluation of the X-ray attenuation intensity was carried out by loading the digital CT images in a standard display program and then selecting a uniform round region of interest on the resultant CT image for each sample. Contrast enhancement was determined in Hounsfield units (HU) for each sample with different Au concentrations.

Hemolysis Assay. Fresh human blood stabilized with heparin was provided by Shanghai First People's Hospital (Shanghai, China). Before the hemolysis assay, the healthy human red blood cells (HRBCs) were acquired according to a protocol reported in the literature.[36] In brief, HRBCs were separated from fresh human blood by centrifugation at 1000 rpm for 10 min and were purified by five successive washes with phosphate buffered saline (PBS). Thereafter, the suspension of HRBCs was 10-fold diluted with PBS. The diluted HRBC suspension (0.1 mL) was then added to water (0.9 mL) as a positive control, PBS (0.9 mL) as a negative control, and PBS (0.9 mL) containing Fe_3O_4@Au CNPs at different concentrations (50−400 μg/mL), respectively. The mixtures were maintained without moving for 2 h at room temperature after an initial gentle shaking. After centrifugation of the samples (10000 rpm, 1 min), the absorbance of the supernatants (hemoglobin) was recorded by a PerkinElmer Lambda 25 UV−vis spectrophotometer, and the digital pictures of the samples were taken. The hemolysis percentages (HPs) of the samples were calculated according to the following equation

$$\mathrm{HP}\ (\%) = \frac{D_t - D_{nc}}{D_{pc} - D_{nc}} \times 100 \quad (1)$$

where D_t is the absorbance of the test samples at 541 nm and D_{pc} and D_{nc} are the absorbance of the positive and negative controls at 541 nm, respectively.

Cytotoxicity Assays and Cell Morphology Observation. KB cells were regularly cultured in 25 cm^2 plates in RPMI 1640 medium containing 10% heat-inactivated fetal bovine serum (FBS), penicillin (100 U/mL), and streptomycin (100 U/mL) under 37 °C and 5% CO_2. The viability of the cells treated with the Fe_3O_4@Au CNPs at

different concentrations was quantified via MTT assay. Briefly, 1×10^4 cells per well were seeded into a 96-well plate with 200 μL of RPMI 1640 medium. The next day the cell medium was substituted with fresh medium (200 μL) that contained pure PBS (control) and Fe_3O_4@Au CNPs at different concentrations (10, 25, 50, 75, and 100 μg/mL, respectively). MTT solution (20 μL, 0.5 mg/mL in PBS) was added to each well after 24 h of culture at 37 °C and 5% CO_2. The assays were carried out according to the manufacturer's instructions. The absorbance of each well was recorded using a Thermo Scientific Multiskan MK3 ELISA reader at 570 nm. For each sample, the mean value and standard deviation of five parallel wells were reported.

After treatment with PBS and Fe_3O_4@Au CNPs at different concentrations (10, 25, 50, 75, and 100 μg/mL, respectively) for 24 h, the cell morphology was observed by phase contrast microscopy (Leica DM IL LED inverted phase contrast microscope) to assess the cytotoxicity of the CNPs. For each sample, the magnification was set at 200 ×.

The cytotoxicity of the Fe_3O_4@Au CNPs was further examined by flow cytometry. KB cells at a density of 2×10^5 cells per well were seeded in 12-well cell culture plates and allowed to grow at 37 °C and 5% CO_2 overnight. After replacing the medium with fresh medium containing different concentrations of CNPs (10, 25, 50, 75, and 100 μg/mL, respectively), the cells were then incubated at 37 °C and 5% CO_2 for 24 h. Afterwards, the cells were harvested by trypsinization and centrifugation and then resuspended in 1 mL of PBS. The cell suspensions were stained with 0.4 μL FDA (0.5 mg/mL) for 5 min and then analyzed by flow cytometry (FACS-Calibur, Becton Dickinson) in the FL1 channel at 488 nm. For each sample, 1×10^4 cells were counted, and the measurement was repeated three times.

In Vivo MR and CT Imaging. All animal experiments were performed according to protocols approved by the institutional ethical committee for animal care, and also were in accordance with the policy of the National Ministry of Health. For mouse liver MR imaging, after the C57 mice (40−45 g, Shanghai SLAC Laboratory Animal Center, Shanghai, China) were anesthetized by an intraperitoneal injection of pentobarbital sodium (40 mg/kg), a PBS solution containing Fe_3O_4@Au CNPs (0.3 mL, [Fe] = 129.17 mM, [Au] = 68.46 mM) was intravenously injected into the mice via the tail vein. A 3.0 T Signa HDxt superconductor clinical MR system with a custom-built rodent receiver coil (Chenguang Med Tech, Shanghai, China) was employed to image the mice, which were placed inside the MR receiver coil. For each animal, 2D spin-echo T_2-weighted MR images were collected at each time point with 2 mm slice thickness, 2000/81.9 ms TR/TE, 6 × 6 cm FOV, and 256 × 160 matrix. Two-dimensional MR images were obtained both before and after administration of the Fe_3O_4@Au CNPs at different time points (0.5, 1, 2, and 4 h). To acquire the 2D images, 2.2 min was required.

Sprague-Dawley rats (250−300 g, Shanghai SLAC Laboratory Animal Center, Shanghai, China) were used for blood pooling and liver CT imaging. After the rats were anesthetized by an intraperitoneal injection of pentobarbital sodium (40 mg/kg), a PBS solution containing Fe_3O_4@Au CNPs (1.0 mL, [Fe] = 129.17 mM, [Au] = 68.46 mM) was injected into the rats via the tail vein. A GE LightSpeed VCT clinical imaging system (GE Medical Systems) was used for CT scanning with 100 kV, 80 mA, and a slice thickness of 0.625 mm at 1 and 20 min postinjection. A GE Advantage Workstation AW4.4 (GE Medical Systems) was used to reconstruct the images.

In Vivo Biodistribution. The C57 mice (40−45 g) were used to examine the in vivo biodistribution of the Fe_3O_4@Au CNPs. The mice were first anesthetized by an intraperitoneal injection of pentobarbital sodium (40 mg/kg). A PBS solution containing Fe_3O_4@Au CNPs (0.3 mL, [Fe] = 129.17 mM, [Au] = 68.46 mM) was then intravenously injected into the mice via the tail vein. The mice were euthanized, and the heart, liver, spleen, lung, kidney, stomach, brain, and muscle were extracted and weighed at different time points (1, 4, 12, and 24 h postinjection). The organs were then cut into small pieces (1 to 2 mm^2) and digested by aqua regia for 2 days before ICP−AES analysis.

RESULTS AND DISCUSSION

Synthesis and Characterization of Fe_3O_4@Au CNPs. In our previous work, we prepared a nanocomposite particle system by incorporating both preformed Fe_3O_4 NPs and Au NPs via dendrimer-mediated LbL self-assembly.[47] Unlike the self-assembly approach that required both preformed Fe_3O_4 NPs and Au NPs and multiple assembly steps, in this study we used a facile one-pot hydrothermal approach to form Fe_3O_4@Au CNPs in which preformed Fe_3O_4 NPs are not required but preformed *m*PEG-PEI.NH_2-Au NPs are required (Scheme 1).

To form *m*PEG-PEI.NH_2-Au NPs, PEI partially modified with *m*PEG (*m*PEG-PEI.NH_2) was first synthesized and characterized by ^{1}H NMR spectroscopy (Figure S1, Supporting Information). On the basis of a careful calculation of the NMR integration, the average number of *m*PEG linked to each PEI was estimated to be 10. The *m*PEG-PEI.NH_2 conjugate was then used as a stabilizer to form Au NPs (*m*PEG-PEI.NH_2-Au NPs) with the assistance of $NaBH_4$ reduction. The initial light-yellow color of the $HAuCl_4$/*m*PEG-PEI.NH_2 mixture solution changed to deep red rapidly, indicating the formation of Au NPs. On the basis of TEM characterization (Figure S2, Supporting Information), the formed *m*PEG-PEI.NH_2-Au NPs have a spherical shape, are highly crystalline because lattices of Au crystals can be seen from a typical high-resolution TEM image, and are quite uniform, with a mean diameter of 3.5 ± 0.7 nm.

Next, in the presence of *m*PEG-PEI.NH_2-Au NPs, a hydrothermal approach was used to generate Fe_3O_4@Au-*m*PEG-PEI.NH_2 CNPs. After the synthesis, the color of the product changed to dark blue. A final step of acetylation to neutralize the remaining PEI surface amines did not cause any color change of the CNP suspension. UV−vis spectrometry was used to confirm the formation of the *m*PEG-PEI.NH_2-Au NPs, Fe_3O_4@Au-*m*PEG-PEI.NH_2 CNPs, and final Fe_3O_4@Au CNPs (Figure S3, Supporting Information). It is clear that the formed *m*PEG-PEI.NH_2-Au NPs display a surface plasmon resonance (SPR) peak at around 520 nm, indicating the formation of Au NPs (curve a). In contrast, the Fe_3O_4-PEI NPs synthesized in the absence of *m*PEG-PEI.NH_2-Au NPs according to our previous work[33] do not show any obvious features in the same region (curve d). The SPR peak of both Fe_3O_4@Au-*m*PEG-PEI.NH_2 CNPs and Fe_3O_4@Au CNPs shows a red shift to 540 nm (curves b and c, respectively), confirming the formation of the CNP structure.[53−55] In agreement with the product color change, the acetylation reaction does not seem to alter the SPR peak position (curve c), indicative of the good stability of the formed CNPs.

The crystalline structure of the formed Fe_3O_4@Au CNPs was characterized by XRD (Figure 1). The lattice spacing calculated from the diffraction peaks observed at 30.2, 35.4, 43.5, 53.4, 57.1, and 62.7° well matches the [220], [311], [400], [422], [511], and [440] planes of Fe_3O_4 crystals, respectively. Five additional peaks at 38.1, 44.2, 64.6, 77.5 and 81.8° can be assigned to the [111], [200], [220], [311], and [222] planes of the Au crystals. The XRD pattern confirms the presence of both Fe_3O_4 and Au crystals in the formed Fe_3O_4@Au CNP structure. The composition of the formed Fe_3O_4@Au CNPs was further analyzed by TGA (Figure S4, Supporting Information). The weight loss of both the Fe_3O_4@Au-*m*PEG-PEI.NH_2 CNPs and Fe_3O_4@Au CNPs in a temperature range of 25−200 °C can be ascribed to the loss of moisture in the samples. For Fe_3O_4@Au-*m*PEG-PEI.NH_2 CNPs, the final

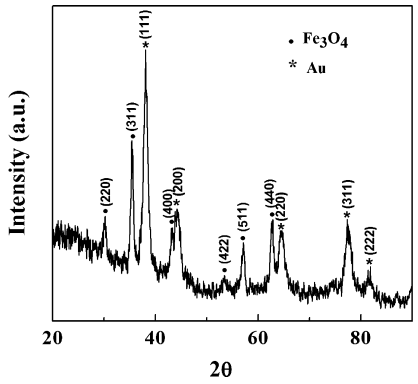

Figure 1. XRD pattern of the formed Fe_3O_4@Au CNPs.

weight loss was estimated to be about 15.14%, suggesting the successful coating of *m*PEG-PEI.NH_2 onto the surface of CNPs. After the acetylation reaction, the Fe_3O_4@Au CNPs show a weight loss of 17.71%. The increased weight loss should be due to the molecular weight increase after the transformation of *m*PEG-PEI.NH_2 to *m*PEG-PEI.NHAc. The TGA result indicates that the remaining PEI amines on the surface of the CNPs have been successfully acetylated. The surface potential alteration before and after acetylation modification of the CNPs was also characterized by zeta potential measurements (Table 1). We can see that the surface potential of the positively charged Fe_3O_4@Au-*m*PEG-PEI.NH_2 CNPs (+27.4 mV) is decreased to +12.8 mV after the acetylation reaction. It appears that the acetylation reaction is not able to completely neutralize the positive surface charges of the Fe_3O_4@Au CNPs, even in the presence of a much greater molar excess of acetic anhydride. This may be ascribed to the fact that a portion of the PEI surface amines used to stabilize the CNPs are not able to be acetylated, in agreement with our previous work.[33] The hydrodynamic size of the Fe_3O_4@Au-*m*PEG-PEI.NH_2 and Fe_3O_4@Au CNPs was analyzed with dynamic light scattering (Table 1). It can be seen that the CNPs before and after acetylation have approximately similar hydrodynamic sizes (263.1 vs 262.7 nm, respectively). Furthermore, our results show that the hydrodynamic sizes of both CNPs do not have any prominent changes (size alteration <15 nm) over a period of 1 week (Figure S5, Supporting Information), demonstrating that the formed CNPs have good colloidal stability in water. The colloidal stability of the Fe_3O_4@Au CNPs was further assessed by dispersing them in different media including water, PBS, and cell culture medium. We show that the CNPs are colloidally stable and that no precipitation occurs in these media for at least 1 month (Figure S6, Supporting Information).

Table 1. Zeta Potential, Hydrodynamic Size, and Polydispersity of Fe_3O_4@Au-*m*PEG-PEI.NH_2 and Fe_3O_4@Au CNPs[a]

materials	zeta potential (mV)	hydrodynamic size (nm)	polydispersity index (PDI)
Fe_3O_4@Au-*m*PEG-PEI.NH_2	27.4 ± 0.45	263.1 ± 2.82	0.54 ± 0.013
Fe_3O_4@Au CNPs	12.8 ± 0.34	262.7 ± 3.06	0.29 ± 0.021

[a]The data are provided as the mean ± SD. (n = 3).

The morphology and size of the Fe_3O_4@Au CNPs were then characterized by TEM imaging (Figures 2 and S7, Supporting Information). It can be clearly seen that some darkened Au nanocrystals with a mean size of 3.5 nm (Figure S2, Supporting Information) are surrounded on the surface of Fe_3O_4 core NPs with a size of around 16.7 nm.[33] The TEM data reveal that the coating of the Au NPs on the surface of the Fe_3O_4 core NPs is not uniform (Figure 2a), similar to that reported in our previous report.[47] In the TEM image, some aggregated or interconnected particles appeared. This could be due to the TEM sample preparation process, which includes the air-drying of the aqueous suspension of the samples. The air-drying process often leads to the aggregation or interconnection of the particles shown in TEM images, which can be commonly seen for Fe_3O_4 NPs or Fe_3O_4-based composite NPs formed by a hydrothermal synthesis route.[2,33,34,48] Energy-dispersive spectroscopy (EDS) data indicate the existence of Cu, O, Fe, and Au elements in the sample of Fe_3O_4@Au CNPs, confirming the formation of Fe_3O_4@Au CNPs (Figure 2b). The presence of Cu should be assigned to the copper grid used for the TEM sample preparation. The crystalline nature of the Fe_3O_4@Au CNPs was further confirmed by high-resolution TEM (Figure S7a) and selected-area electron diffraction (SAED) (Figure S7b), where lattices of Fe_3O_4 and Au crystals are clearly observed in the TEM image, and the SAED rings can be assigned to crystals of both Fe_3O_4 and Au NPs.

Furthermore, the metal composition of the Fe_3O_4@Au CNPs was quantitatively determined by ICP–AES. The Fe_3O_4/Au molar ratio of the product was estimated to be 1:1.59. It should be noted that the gold content in the formed Fe_3O_4@Au CNPs in this work is much higher than that of the Fe_3O_4@

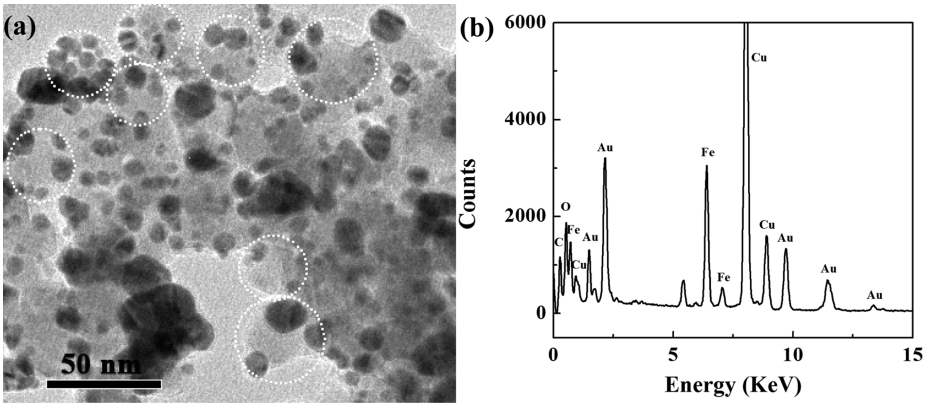

Figure 2. TEM micrograph (a) and EDS spectrum (b) of the Fe_3O_4@Au CNPs.

Au CNPs formed via a self-assembly approach reported in our previous report.[47] Therefore, with the increased Au content in the CNPs, the formed particles may be used as a contrast agent for dual-mode MR/CT imaging applications with improved CT imaging sensitivity.

T_2-Weighted MR Relaxometry and X-ray Attenuation Property. Fe_3O_4 NPs are known to be used as a T_2-weighted MR contrast agent. To demonstrate their uses for MR imaging, T_2-weighted MR relaxometry of the Fe_3O_4@Au CNPs was examined (Figure 3a). It is clear that the MR signal intensity

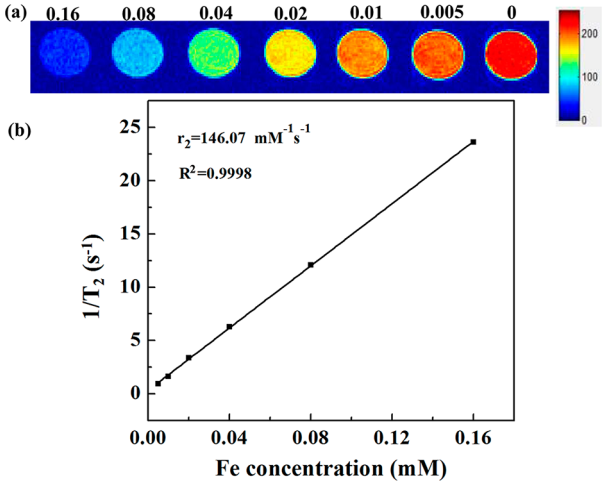

Figure 3. Colored T_2-weighted MR image (a) and linear fitting of $1/T_2$ (b) of the Fe_3O_4@Au CNPs with different Fe concentrations (0.005, 0.01, 0.02, 0.04, 0.08, 0.16 mM, respectively). The color bar from red to blue indicates the gradual decrease of the MR signal intensity.

decreases with the increase of the Fe concentration. By plotting the T_2 relaxation rate ($1/T_2$) as a function of the Fe concentration (Figure 3b), it can be seen that the relaxation rate increases linearly with the Fe concentration with a slope (r_2) of 146.07 mM^{-1} s^{-1}, which is much higher than that of Fe_3O_4@Au CNPs reported in the literature.[16,47,56] Our results suggest that the Fe_3O_4@Au CNPs could be used as a T_2-shortening agent for MR imaging applications.

Au NPs have been widely used as CT contrast agents because of their better X-ray attenuation property than conventional iodine-based small-molecule CT contrast agents.[10,23,25,40,41] To explore the CT imaging potential, the X-ray attenuation property of the formed Fe_3O_4@Au CNPs was explored (Figure 4). It is clear that the intensity of the CT image increases with the Au concentration (Figure 4a). By plotting the CT value (in HU) of the CNPs as function of the Au concentration (Figure 4b), we can see a linear increase of the CT value of Fe_3O_4@Au CNPs with the Au concentration, in agreement with our previous report.[47] A careful comparison with the X-ray attenuation property of a conventional CT contrast agent Omnipaque reported in our previous work[43,57,58] revealed that the attenuation intensity of the Fe_3O_4@Au CNPs is much higher than that of Omnipaque under similar Au or iodine concentrations. A good X-ray attenuation property of the CNPs is essential for their uses as contrast agents in sensitive CT imaging applications.

Hemolytic Assay of Fe_3O_4@Au CNPs. Hemocompatibility is an important issue for a NP system to be used for biomedical applications, especially in the circumstances

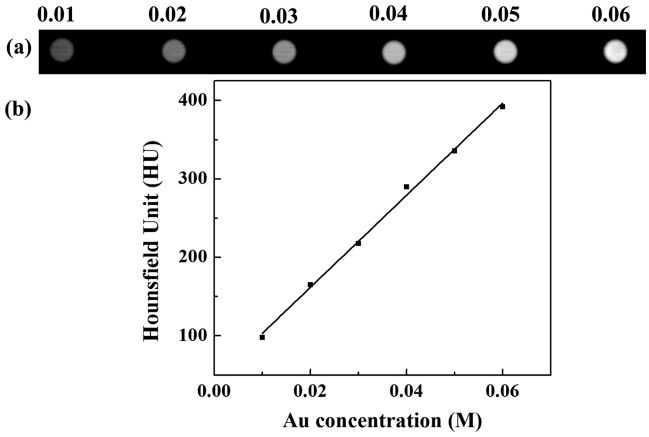

Figure 4. CT image of the Fe_3O_4@Au CNPs under different Au concentrations (0.01, 0.02, 0.03, 0.04, 0.05, 0.06 M, respectively) (a) and the X-ray attenuation intensity of the Fe_3O_4@Au CNPs as a function of the Au concentration (b).

requiring the NPs to contact blood. The hemolysis activity of the Fe_3O_4@Au CNPs was examined before their uses as a contrast agent for dual-mode MR/CT imaging (Figure 5). In

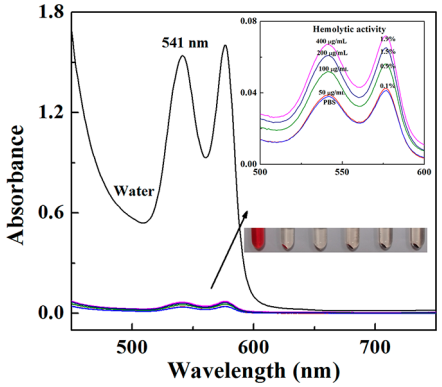

Figure 5. Hemolytical activity of the Fe_3O_4@Au CNPs at different concentrations (50, 100, 200, and 400 μg/mL, respectively). PBS and water were used as negative and positive controls, respectively. The bottom right inset shows the photograph of HRBCs exposed to water, PBS, and PBS containing CNPs with a concentration of 50, 100, 200, and 400 μg/mL (from left to right), respectively, for 2 h followed by centrifugation. The top right inset shows the enlarged UV−vis spectra (as indicated by the arrow).

contrast to the positive control (water), the CNPs do not display any visible hemolytic effect in a concentration range of 0−400 μg/mL (bottom right inset of Figure 5). The hemolysis effect of the CNPs was also quantified on the basis of the hemoglobin absorbance at 541 nm. We show that the hemolysis percentages of the Fe_3O_4@Au CNPs are less than 5% and that the highest hemolysis percentage is 1.9% at the CNP concentration of 400 μg/mL (top right inset of Figure 5). Our results reveal that the developed Fe_3O_4@Au CNPs have an excellent hemocompatibility, which is important for their further biomedical applications.

Cytotoxicity Assay and Cell Morphology Observation. We next explored the cytotoxicity of the Fe_3O_4@Au CNPs before they were used for in vivo imaging applications. After incubation with Fe_3O_4@Au CNPs at different concentrations (10, 25, 50, 75, and 100 μg/mL, respectively) for 24 h, an MTT viability assay of KB cells was carried out (Figure 6). It can be

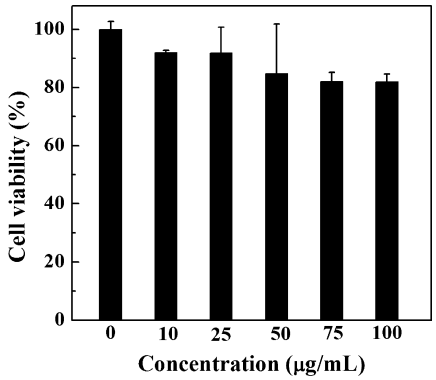

Figure 6. MTT assay of KB cell viability after treatment with Fe_3O_4@Au CNPs at concentrations of 0−100 μg/mL for 24 h. KB cells treated with PBS were used as the control.

seen that the viability of the cells after treatment with Fe_3O_4@Au CNPs in the studied concentration range is quite similar to the PBS control. Our data clearly suggest that the formed Fe_3O_4@Au CNPs have a good cytocompatibility at a concentration up to 100 μg/mL.

The cytotoxicity of the Fe_3O_4@Au CNPs was then assessed by observation of the morphology of KB cells treated with the CNPs at the concentrations of 10, 25, 50, 75, and 100 μg/mL for 24 h by optical microscopy (Figure S8, Supporting Information). It is clear that the cells do not display any appreciable morphological changes at concentrations up to 100 μg/mL when compared with the control cells treated with PBS. These results corroborate the above MTT assay data, suggesting that the CNPs have a good cytocompatibility in the given concentration range.

The cytocompatibility of the Fe_3O_4@Au CNPs was further confirmed by flow cytometric analysis of the cells treated with the CNPs at different concentrations for 24 h (Figure 7). In the flow cytometric analysis, living cells were stained with FDA after treatment with PBS and Fe_3O_4@Au CNPs at different concentrations. KB cells treated with PBS without FDA staining was used as the control (Figure 7a). It can be seen that the flow cytometric analysis is not valid for living KB cells without FDA staining. For the FDA-stained KB cells treated with PBS, the percentage of living cells was estimated to be 96.85% (Figure 7b). Similarly, KB cells treated with the CNPs at concentrations of 10, 25, 50, 75, and 100 μg/mL have 94.04, 92.12, 90.66, 89.05, and 88.16% FDA-stained populations, respectively (Figure 7c−g). Taken together with the results from MTT assay and cell morphology observation, our results suggest that the Fe_3O_4@Au CNPs are cytocompatible in the studied concentration range, which is essential for their in vivo MR/CT imaging applications.

In Vivo MR and CT Imaging. The high T_2 relaxivity and excellent X-ray attenuation property of the formed Fe_3O_4@Au CNPs along with their good cytocompatibility and hemocompatibility prompted us to explore further their uses as a contrast agent for in vivo dual-mode MR/CT imaging applications. After intravenous injection of the Fe_3O_4@Au CNPs (0.3 mL, [Fe] = 129.17 mM, [Au] = 68.46 mM) into mice via the tail vein, MR scans were performed. Figure 8a shows the in vivo T_2-weighted MR images of the mouse liver before and after intravenous administration of Fe_3O_4@Au CNPs at time points of 0.5, 1, 2, and 4 h, respectively. It is clear that the liver region (indicated by the white star) dramatically darkened and became the darkest at 0.5 h postinjection. The liver then started to

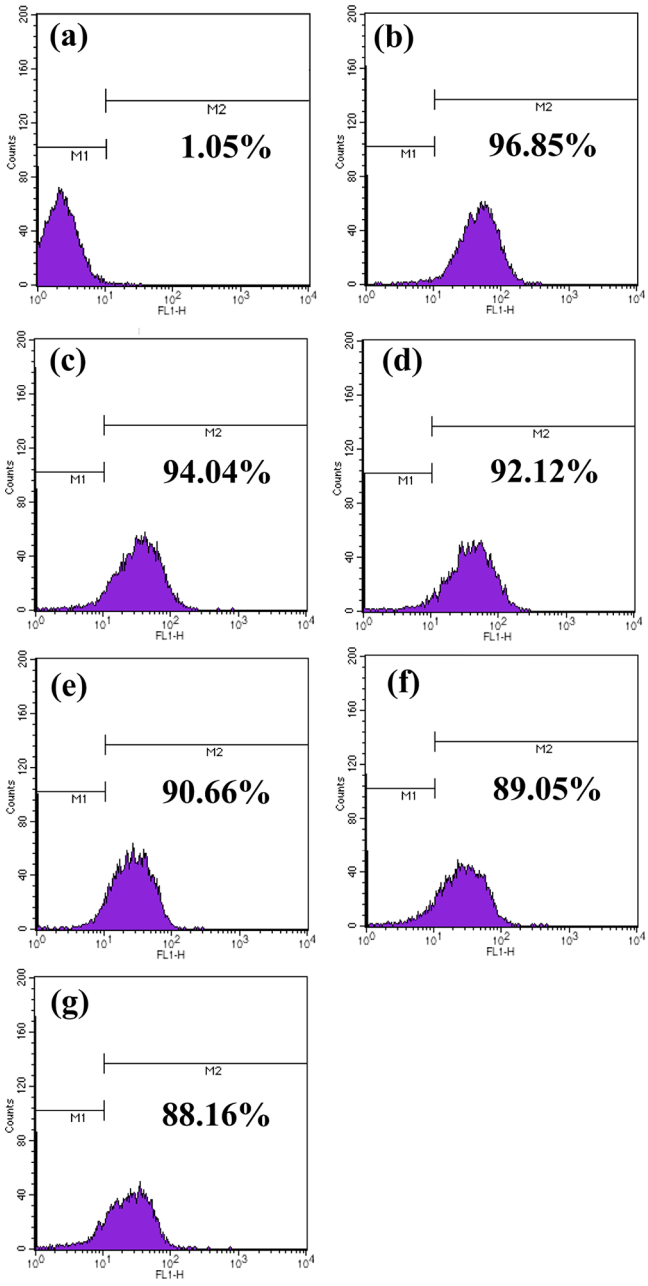

Figure 7. Flow cytometric analysis of KB cells treated with PBS without FDA staining (a), KB cells treated with PBS with FDA staining (b), and FDA-stained KB cells treated with Fe_3O_4@Au CNPs at concentrations of 10 (c), 25 (d), 50 (e), 75 (f), and 100 μg/mL (g) for 24 h (n = 3). The percentage value shown in each panel indicates the FDA-stained cell population.

become bright at 1 h postinjection, which is probably due to the Fe_3O_4@Au CNPs undergoing a further metabolism process and having a decreased Fe concentration in the liver with time. Consequently, the MR signal intensity gradually recovered. The quantitative signal intensity change of liver as a function of time postinjection of the Fe_3O_4@Au CNPs can be seen in Figure 8b. At 0.5 h postinjection, the mouse liver shows a significantly reduced T_2 MR signal intensity (2453.30) when compared to the initial signal before injection (6603.65). Subsequently, the signal intensity gradually recovered to 3519.80, 4076.30, and 5522.00 at 1, 2, and 4 h postinjection, respectively. Our results

dx.doi.org/10.1021/am4034526 | ACS Appl. Mater. Interfaces 2013, 5, 10357−10366

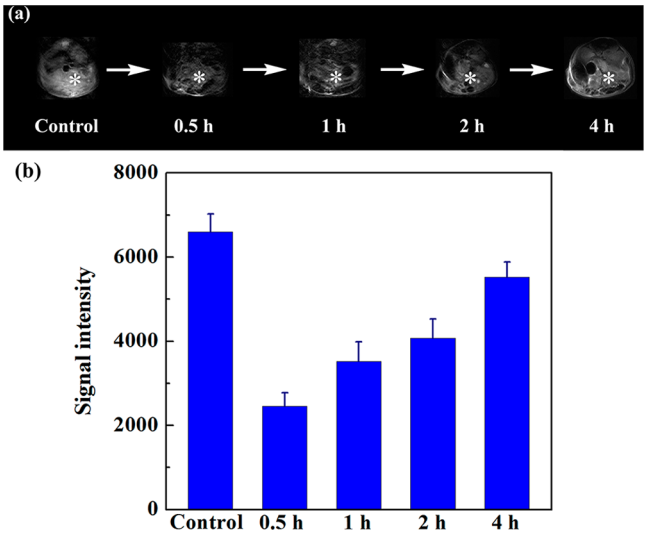

Figure 8. T_2-weighted MR images (a) and signal intensity (b) of the mouse liver before injection and at different time points after intravenous injection of Fe_3O_4@Au CNPs (0.3 mL in PBS, [Fe] = 129.17 mM, [Au] = 68.46 mM).

show that the formed Fe_3O_4@Au CNPs can be used as a T_2 negative contrast agent for in vivo mouse liver MR imaging.

We next explored the CT imaging capability of the Fe_3O_4@Au CNPs by intravenously injecting them (1.0 mL in PBS, [Fe] = 129.17 mM, [Au] = 68.46 mM) into rats via the tail vein. CT images were collected at different time points postinjection (Figure 9). From Figure 9a, as indicated by the red arrow, it can be seen that the administration of the Fe_3O_4@Au CNPs enables a clear CT contrast enhancement of the aorta. Similarly, as the white star indicates, the whole liver became more clear and sharp at 20 min postinjection. To quantify the CT imaging enhancement, the CT values of the liver and aorta were measured at different time points (Figure 9b). The CT values of the liver and aorta were estimated to be 73.9 and 81 HU at 1 min postinjection, respectively, much higher than the initial respective values of 60.9 and 58 HU before injection. Because of the metabolism of the Fe_3O_4@Au CNPs in the rats, the CT value of the liver increased to 86.6 HU, whereas the contrast enhancement of the aorta was slightly weakened, with a CT value of 78 HU at 20 min postinjection.

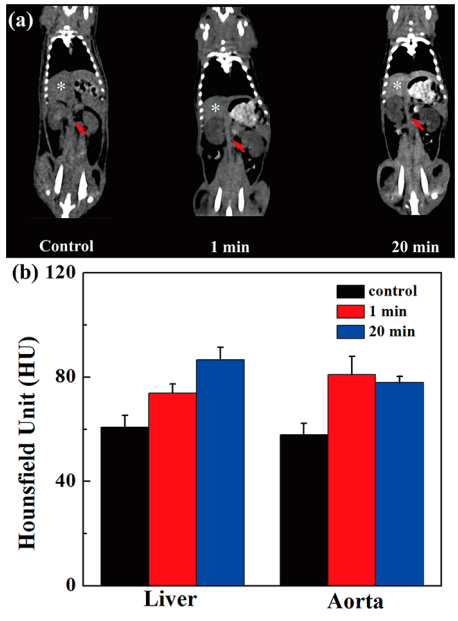

Figure 9. CT images (a) and CT values (HU) (b) of rat liver and aorta before injection and at different time points after intravenous injection of Fe_3O_4@Au CNPs (1.0 mL in PBS, [Fe] = 129.17 mM, [Au] = 68.46 mM).

Overall, our results suggest that the developed Fe_3O_4@Au CNPs can be used as a contrast agent for dual-mode MR/CT imaging applications. It should be noted that the mice and rats behaved normally and that no undesirable side effects were observed after the injection of the CNPs, similar to those without injection. This further suggests that the injected Fe_3O_4@Au CNPs do not display any appreciable in vivo toxicity.

In Vivo Biodistribution. For further in vivo biomedical imaging applications, it is crucial to confirm the tissue/organ distribution behavior of the Fe_3O_4@Au CNPs. The biodistribution of Fe and Au in different organs of the mice at 1, 4, 12, and 24 h after intravenous injection was quantified by ICP–AES (Figure 10). We can clearly see that at 1 h postinjection,

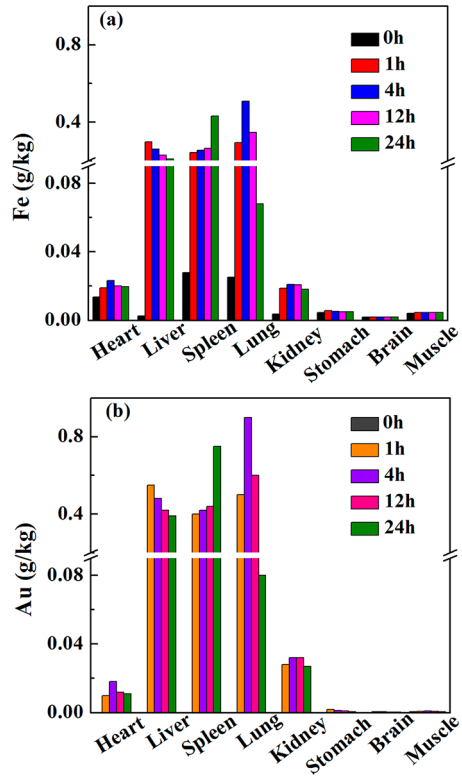

Figure 10. Biodistribution of Fe (a) or Au (b) in the major organs of the mice, including the heart, liver, spleen, lung, kidney, stomach, brain, and muscle at different time points after the intravenous injection of Fe_3O_4@Au CNPs (0.3 mL in PBS, [Fe] = 129.17 mM, [Au] = 68.46 mM).

the liver, spleen, and lung have an Fe uptake of 298.1, 242.8, and 294.0 mg/kg, respectively (Figure 10a). Usually, the intravenously injected NPs can be rapidly cleared from the blood, taken up by the liver, and finally accumulated in the spleen and kidney. Therefore, at 1 h postinjection, we can see that the Fe concentration in the liver starts to decrease, and it increases in the spleen, lung, and kidney at 4 h postinjection.

dx.doi.org/10.1021/am4034526 | ACS Appl. Mater. Interfaces 2013, 5, 10357–10366

The quite high lung uptake may indicate the possible aggregation of CNPs in the plasma after intravenous injection. Improving the surface modification of the CNPs or seeking an optimized strategy to reduce the size of the CNPs may be necessary in our future study. With prolonged circulation time, the CNPs began to be cleared from the lung and kidney and gradually accumulated in the spleen. At all of the time points, only a very small amount of Fe remained in the other organs, such as the heart, stomach, muscle, and brain. It is worth noting that the Au uptake data (Figure 10b) show a similar trend in the distribution of different organs to those of Fe uptake, further demonstrating that the formed Fe_3O_4@Au CNPs in our study are indeed one integrated particle system rather than the physical mixture of Fe_3O_4 NPs and Au NPs. Future pharmacokinetic studies of the Fe_3O_4@Au CNPs over extended time periods are important for a better understanding of the biodistribution of the CNPs.

CONCLUSIONS

We developed a facile one-pot hydrothermal approach to fabricating Fe_3O_4@Au CNPs for dual-mode MR/CT imaging applications. The formed Fe_3O_4@Au CNPs have good water dispersibility, colloidal stability, hemocompatibility, and cytocompatibility in the given concentration range. The T_2 relaxometry and X-ray attenuation measurements show that the Fe_3O_4@Au CNPs have a high r_2 relaxivity of 146.07 mM^{-1} s^{-1} and a good X-ray attenuation property as a result of the coexistence of Fe_3O_4 NPs and Au NPs. These properties enable the use of the Fe_3O_4@Au CNPs as a contrast agent for dual-mode MR/CT imaging applications, which has been demonstrated by the MR imaging of mouse liver and CT imaging of rat liver and aorta. We are currently using the developed Fe_3O_4@Au CNPs as contrast agents for tumor imaging via an enhanced permeability and retention effect. Taking into consideration of the numerous amines on the surface of the PEI that can be further modified with different targeting ligands, it is expected that multifunctional Fe_3O_4@Au CNPs may be developed for targeted MR/CT dual-mode imaging of different biological systems, especially for high-accuracy early-stage diagnosis of cancer.

ASSOCIATED CONTENT

Supporting Information

^{1}H NMR spectrum of *m*PEG-PEI.NH_2; TEM images and size distribution histogram of the formed *m*PEG-PEI.NH_2-Au NPs; UV−vis spectra of the *m*PEG-PEI.NH_2-Au NPs, Fe_3O_4@Au-*m*PEG-PEI.NH_2 CNPs, Fe_3O_4@Au CNPs, and Fe_3O_4-PEI NPs; TGA curves of the Fe_3O_4@Au-*m*PEG-PEI.NH_2 CNPs and the Fe_3O_4@Au CNPs; change in the hydrodynamic size of the Fe_3O_4@Au-*m*PEG-PEI.NH_2 CNPs (before acetylation) and Fe_3O_4@Au CNPs (after acetylation) as a function of storage time; photos of Fe_3O_4@Au CNPs dispersed in water, PBS, and cell culture medium; high-resolution TEM image and selected area electron diffraction pattern of the Fe_3O_4@Au CNPs, and phase contrast microscopic images of KB cells treated with PBS or Fe_3O_4@Au CNPs. This material is available free of charge via the Internet at http://pubs.acs.org.

AUTHOR INFORMATION

Corresponding Authors

*E-mail: mwshen@dhu.edu.cn (M.S.).
*E-mail: guixiangzhang@sina.com (G.Z.).
*E-mail: xshi@dhu.edu.cn (X.S.).

Author Contributions

⊥These authors contributed equally to this work.

Notes

The authors declare no competing financial interest.

ACKNOWLEDGMENTS

This research is financially supported by the Fund of the Science and Technology Commission of Shanghai Municipality (11nm0506400 to X.S. and 12520705500 to M.S.), the National Natural Science Foundation of China (81101150, 21273032, and 81271384), the Program for Professor of Special Appointment (Eastern Scholar) at Shanghai Institutions of Higher Learning, and the Program for New Century Excellent Talents in University, State Education Ministry. X.S. gratefully acknowledges the Fundação para a Ciência e a Tecnologia (FCT) through the Strategic Plan PEst-OE/QUI/UI0674/2011 as well as the FCT and Santander bank for the Invited Chair in Nanotechnology.

REFERENCES

(1) Bae, K. H.; Kim, Y. B.; Lee, Y.; Hwang, J. Y.; Park, H. W.; Park, T. G. *Bioconjugate Chem.* **2010**, *21*, 505.
(2) Shi, X.; Wang, S. H.; Swanson, S. D.; Ge, S.; Cao, Z.; Van Antwerp, M. E.; Landmark, K. J.; Baker, J. R. *Adv. Mater.* **2008**, *20*, 1671.
(3) Xie, J.; Chen, K.; Lee, H. Y.; Xu, C.; Hsu, A. R.; Peng, S.; Chen, X.; Sun, S. *J. Am. Chem. Soc.* **2008**, *130*, 7542.
(4) Yang, H.; Zhuang, Y.; Sun, Y.; Dai, A.; Shi, X.; Wu, D.; Li, F.; Hu, H.; Yang, S. *Biomaterials* **2011**, *32*, 4584.
(5) Almutairi, A.; Rossin, R.; Shokeen, M.; Hagooly, A.; Ananth, A.; Capoccia, B.; Guillaudeu, S.; Abendschein, D.; Anderson, C. J.; Welch, M. J. *Proc. Natl. Acad. Sci. U.S.A.* **2009**, *106*, 685.
(6) Amirkhanov, N. V.; Zhang, K.; Aruva, M. R.; Thakur, M. L.; Wickstrom, E. *Bioconjugate Chem.* **2010**, *21*, 731.
(7) Cai, Q.-Y.; Kim, S. H.; Choi, K. S.; Kim, S. Y.; Byun, S. J.; Kim, K. W.; Park, S. H.; Juhng, S. K.; Yoon, K.-H. *Invest. Radiol.* **2007**, *42*, 797.
(8) Guo, R.; Wang, H.; Peng, C.; Shen, M.; Pan, M.; Cao, X.; Zhang, G.; Shi, X. *J. Phys. Chem. C* **2009**, *114*, 50.
(9) Peng, C.; Wang, H.; Guo, R.; Shen, M.; Cao, X.; Zhu, M.; Zhang, G.; Shi, X. *J. Appl. Polym. Sci.* **2010**, *119*, 1673.
(10) Peng, C.; Zheng, L.; Chen, Q.; Shen, M.; Guo, R.; Wang, H.; Cao, X.; Zhang, G.; Shi, X. *Biomaterials* **2012**, *33*, 1107.
(11) Fang, N.; Lee, H.; Sun, C.; Zhang, X. *Science* **2005**, *308*, 534.
(12) Sokolov, K.; Follen, M.; Aaron, J.; Pavlova, I.; Malpica, A.; Lotan, R.; Richards-Kortum, R. *Cancer Res.* **2003**, *63*, 1999.
(13) Wagner, A.; Mahrholdt, H.; Holly, T. A.; Elliott, M. D.; Regenfus, M.; Parker, M.; Klocke, F. J.; Bonow, R. O.; Kim, R. J.; Judd, R. M. *Lancet* **2003**, *361*, 374.
(14) Xu, X.; Zhang, Y.; Wang, X.; Guo, X.; Zhang, X.; Qi, Y.; Shen, Y. M. *Bioorg. Med. Chem.* **2011**, *19*, 1643.
(15) Zhang, Y.; Sun, Y.; Xu, X.; Zhang, X.; Zhu, H.; Huang, L.; Qi, Y.; Shen, Y. M. *J. Med. Chem.* **2010**, *53*, 3262.
(16) Zhou, T.; Wu, B.; Xing, D. *J. Mater. Chem.* **2012**, *22*, 470.
(17) Niedre, M.; Ntziachristos, V. *Proc. − IEEE* **2008**, *96*, 382.
(18) Spernyak, J. A.; White Iii, W. H.; Ethirajan, M.; Patel, N. J.; Goswami, L.; Chen, Y.; Turowski, S.; Missert, J. R.; Batt, C.; Mazurchuk, R. *Bioconjugate Chem.* **2010**, *21*, 828.
(19) Schlemmer, H. P. W.; Pichler, B. J.; Schmand, M.; Burbar, Z.; Michel, C.; Ladebeck, R.; Jattke, K.; Townsend, D.; Nahmias, C.; Jacob, P. K. *Radiology* **2008**, *248*, 1028.
(20) Catana, C.; van der Kouwe, A.; Benner, T.; Michel, C. J.; Hamm, M.; Fenchel, M.; Fischl, B.; Rosen, B.; Schmand, M.; Sorensen, A. G. *J. Nucl. Med.* **2010**, *51*, 1431.
(21) Truong, M. T.; Marom, E. M.; Erasmus, J. J. *J. Thorac. Imaging* **2006**, *21*, 146.

(22) Antoch, G.; Kanja, J.; Bauer, S.; Kuehl, H.; Renzing-Koehler, K.; Schuette, J.; Bockisch, A.; Debatin, J. F.; Freudenberg, L. S. *J. Nucl. Med.* **2004**, *45*, 357.
(23) Chen, Q.; Li, K.; Wen, S.; Liu, H.; Peng, C.; Cai, H.; Shen, M.; Zhang, G.; Shi, X. *Biomaterials* **2013**, *34*, 5200.
(24) Narayanan, S.; Sathy, B. N.; Mony, U.; Koyakutty, M.; Nair, S. V.; Menon, D. *ACS Appl. Mater. Interfaces* **2011**, *4*, 251.
(25) Wen, S.; Li, K.; Cai, H.; Chen, Q.; Shen, M.; Huang, Y.; Peng, C.; Hou, W.; Zhu, M.; Zhang, G. *Biomaterials* **2013**, *34*, 1570.
(26) Luo, T.; Huang, P.; Gao, G.; Shen, G.; Fu, S.; Cui, D.; Zhou, C.; Ren, Q. *Opt. Express* **2011**, *19*, 17030.
(27) Josephson, L.; Kircher, M. F.; Mahmood, U.; Tang, Y.; Weissleder, R. *Bioconjugate Chem.* **2002**, *13*, 554.
(28) Melancon, M. P.; Wang, Y.; Wen, X.; Bankson, J. A.; Stephens, L. C.; Jasser, S.; Gelovani, J. G.; Myers, J. N.; Li, C. *Invest. Radiol.* **2007**, *42*, 569.
(29) Cheng, L.; Yang, K.; Li, Y.; Zeng, X.; Shao, M.; Lee, S.-T.; Liu, Z. *Biomaterials* **2012**, *33*, 2215.
(30) Zhang, W. L.; Li, N.; Huang, J.; Yu, J. H.; Wang, D. X.; Li, Y. P.; Liu, S. Y. *J. Appl. Polym. Sci.* **2010**, *118*, 1805.
(31) Huh, Y.-M.; Jun, Y.-w.; Song, H.-T.; Kim, S.; Choi, J.-s.; Lee, J.-H.; Yoon, S.; Kim, K.-S.; Shin, J.-S.; Suh, J.-S. *J. Am. Chem. Soc.* **2005**, *127*, 12387.
(32) Shi, X.; Gong, H.; Li, Y.; Wang, C.; Cheng, L.; Liu, Z. *Biomaterials* **2013**, *34*, 4786.
(33) Cai, H.; An, X.; Cui, J.; Li, J.; Wen, S.; Li, K.; Shen, M.; Zheng, L.; Zhang, G.; Shi, X. *ACS Appl. Mater. Interfaces* **2013**, *5*, 1722.
(34) Wang, S. H.; Shi, X.; Van Antwerp, M.; Cao, Z.; Swanson, S. D.; Bi, X.; Baker, J. R., Jr. *Adv. Funct. Mater.* **2007**, *17*, 3043.
(35) Li, J.; Zheng, L.; Cai, H.; Sun, W.; Shen, M.; Zhang, G.; Shi, X. *Biomaterials* **2013**, *34*, 8382.
(36) Shen, M.; Cai, H.; Wang, X.; Cao, X.; Li, K.; Wang, S. H.; Guo, R.; Zheng, L.; Zhang, G.; Shi, X. *Nanotechnology* **2012**, *23*, 105601.
(37) Gao, L.; Fei, J.; Zhao, J.; Li, H.; Cui, Y.; Li, J. *ACS Nano* **2012**, *6*, 8030.
(38) Yan, X.; Blacklock, J.; Li, J.; Möhwald, H. *ACS Nano* **2012**, *6*, 111.
(39) Li, D.; He, Q.; Li, J. *Adv. Colloid Interface Sci.* **2009**, *149*, 28.
(40) Wang, H.; Zheng, L.; Peng, C.; Guo, R.; Shen, M.; Shi, X.; Zhang, G. *Biomaterials* **2011**, *32*, 2979.
(41) Wang, H.; Zheng, L.; Peng, C.; Shen, M.; Shi, X.; Zhang, G. *Biomaterials* **2013**, *34*, 470.
(42) Liu, H.; Xu, Y.; Wen, S.; Zhu, J.; Zheng, L.; Shen, M.; Zhao, J.; Zhang, G.; Shi, X. *Polym. Chem.* **2013**, *4*, 1788.
(43) Liu, H.; Xu, Y.; Wen, S.; Chen, Q.; Zheng, L.; Shen, M.; Zhao, J.; Zhang, G.; Shi, X. *Chem.—Eur. J.* **2013**, *19*, 6409.
(44) Xu, C.; Xie, J.; Ho, D.; Wang, C.; Kohler, N.; Walsh, E. G.; Morgan, J. R.; Chin, Y. E.; Sun, S. *Angew. Chem., Int. Ed.* **2008**, *47*, 173.
(45) Zhang, H.; Zhong, X.; Xu, J. J.; Chen, H. Y. *Langmuir* **2008**, *24*, 13748.
(46) Maleki, H.; Simchi, A.; Imani, M.; Costa, B. F. O.; Mahmoudi, M. *J. Magn. Magn. Mater.* **2012**, *324*, 3997.
(47) Cai, H.; Li, K.; Shen, M.; Wen, S.; Luo, Y.; Peng, C.; Zhang, G.; Shi, X. *J. Mater. Chem.* **2012**, *22*, 15110.
(48) Ge, S.; Shi, X.; Sun, K.; Li, C.; Uher, C.; Baker, J. R., Jr; Banaszak Holl, M. M.; Orr, B. G. *J. Phys. Chem. C* **2009**, *113*, 13593.
(49) Tong, W.; Cao, X.; Wen, S.; Guo, R.; Shen, M.; Wang, J.; Shi, X. *Int. J. Nanomed.* **2012**, *7*, 1069.
(50) Wen, S.; Zheng, F.; Shen, M.; Shi, X. *Colloid Surf., A* **2013**, *419*, 80.
(51) Shi, X.; Wang, S.; Meshinchi, S.; Van Antwerp, M. E.; Bi, X.; Lee, I.; Baker, J. R. *Small* **2007**, *3*, 1245.
(52) Liu, H.; Sun, K.; Zhao, J.; Guo, R.; Shen, M.; Cao, X.; Zhang, G.; Shi, X. *Colloid Surf., A* **2012**, *405*, 22.
(53) Goon, I. Y.; Lai, L. M. H.; Lim, M.; Munroe, P.; Gooding, J. J.; Amal, R. *Chem. Mater.* **2009**, *21*, 673.
(54) Umut, E.; Pineider, F.; Arosio, P.; Sangregorio, C.; Corti, M.; Tabak, F.; Lascialfari, A.; Ghigna, P. *J. Magn. Magn. Mater.* **2012**, *324*, 2373.
(55) Zeng, H.; Sun, S. *Adv. Funct. Mater.* **2008**, *18*, 391.
(56) Smolensky, E. D.; Neary, M. C.; Zhou, Y.; Berquo, T. S.; Pierre, V. C. *Chem. Commun.* **2011**, *47*, 2149.
(57) Xiao, T.; Wen, S.; Wang, H.; Liu, H.; Shen, M.; Zhao, J.; Zhang, G.; Shi, X. *J. Mater. Chem. B* **2013**, *1*, 2773.
(58) Zheng, L.; Zhu, J.; Shen, M.; Chen, X.; Baker, J. R., Jr.; Wang, S. H.; Zhang, G.; Shi, X. *Med. Chem. Commun.* **2013**, *4*, 1001.